Alen Grebo[1,*], *Lovre Krstulović-Opara*[1]

Comparison of U-Net-based mapping from DIC-derived effective strain to infrared thermography data and from infrared thermography data to DIC-derived effective strain

[1]University of Split, Faculty of Electrical Engineering Mechanical Engineering and Naval Architecture, Ulica Ruđera Boškovića 32, 21000 Split, Croatia
*Corresponding author: agrebo@fesb.hr

Original scientific paper
Received: July 2, 2026
Accepted: October 20, 2026
https://doi.org/10.65776/ep.21.2.3

This work is licensed under a Creative Commons Attribution 3.0 Unported License.

Abstract

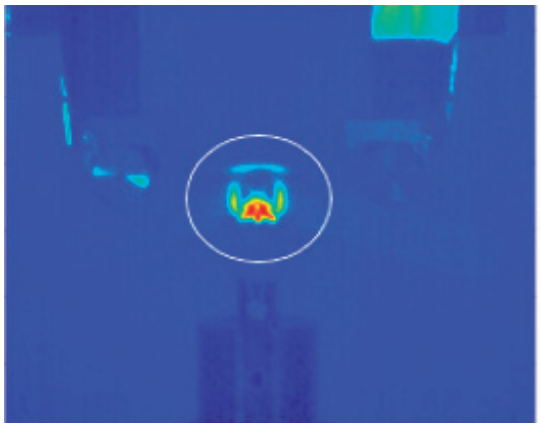
Digital Image Correlation (DIC) and Infrared Thermography (IRT) are complementary full-field techniques used in experimental mechanics for analysing deformation and thermal response during loading. Previous work demonstrated that DIC-derived effective strain fields can be used as input for U-Net-based prediction of corresponding infrared thermography fields. In this paper, that mapping direction is compared with the reverse problem, in which infrared thermography data are used to estimate DIC-derived effective strain fields. Both directions were evaluated using the same paired experimental dataset, consisting of strain and thermal fields obtained from simultaneously recorded mechanical tests. The fields were pre-processed, normalised, resized to 256 × 256 pixels, and used for supervised image-to-image regression.

The results show that both mapping directions can be learned to a certain extent using the same U-Net-based approach, but they are not equivalent. The DIC-to-IRT mapping reproduced the main thermal field distribution and showed stronger structural agreement with the reference thermographic data. The reverse IRT-to-DIC mapping achieved low average pixel-wise errors, with mean RMSE and MAE values of 0.0188 and 0.0051, respectively, but showed limited structural similarity, with a mean SSIM value of 0.0580. This indicates that thermal data contain useful information about the mechanical response, although detailed strain localisation remains difficult to reconstruct. The comparison confirms that the relationship between mechanical and thermal full-field data is direction-dependent and that thermal-to-strain estimation should be interpreted as an approximate complementary approach rather than a replacement for DIC.

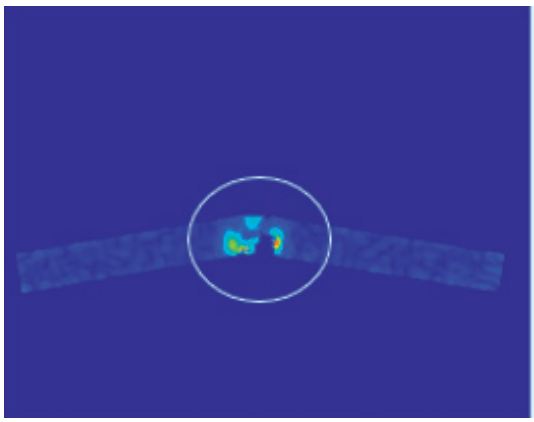
Keywords: *Digital Image Correlation; Infrared Thermography; U-Net; effective strain; image-to-image regression*

1. Introduction

Digital Image Correlation (DIC) and Infrared Thermography (IRT) are widely used full-field methods in experimental mechanics. DIC provides displacement and strain fields by tracking changes in a surface pattern during loading, while IRT records the temperature field on the specimen surface. Since mechanical deformation and thermal response often occur simultaneously, especially during localisation, plastic deformation, damage initiation, or fracture, the two techniques can provide complementary information about the same experiment as can be seen on Fig.1.



a)



b)

Fig. 1. Simultaneously acquired full-field experimental data: (a) infrared thermography image showing the surface temperature field and (b) DIC-derived effective strain field. The highlighted regions indicate the localized thermomechanical response during loading.

In many studies, DIC and IRT are used together to observe the relation between strain development and temperature changes. DIC is commonly used to identify regions of high strain, strain concentration, and crack initiation [1], while IRT can show local heating caused by thermoelastic effects, plastic dissipation, damage processes,

or heat transfer[2]. However, although both methods can be recorded at the same time, the resulting data are often treated separately. The comparison is usually made visually, through selected regions of interest, or by analysing individual time histories, rather than by directly mapping one full-field quantity to the other. Deep learning offers a possible way to study this relation in a more direct form. Convolutional neural networks, and especially encoder–decoder models such as U-Net, are suitable for image-to-image regression because they can learn spatial relations between input and output fields. This is useful in experimental mechanics, where the measured data are often available as images or full-field maps. Instead of using only selected points or averaged values, such models can be trained on paired experimental fields and used to estimate one measured quantity from another.

In previous work, a U-Net-based model was used to map DIC-derived effective strain fields to corresponding infrared thermography data [3]. This showed that, under the investigated experimental conditions, the strain field contains enough spatial information for the model to estimate the associated thermal field. However, this result only covers one mapping direction. The reverse problem is also important: whether infrared thermography data can be used to estimate the DIC-derived effective strain field.

These two problems should not be considered equivalent. Mapping from DIC-derived effective strain to IRT data asks whether the mechanical field can be used to reconstruct the thermal response. On the other hand, mapping from IRT data to DIC-derived effective strain asks whether the thermal response contains enough information to estimate the underlying mechanical field. Both tasks can be treated as image-to-image regression problems, but their physical meaning is different. The thermal field is affected by deformation, but also by heat generation, heat transfer, emissivity, surface conditions, and the time-dependent nature of the experiment. The strain field, in contrast, describes the mechanical response more directly.

The aim of this paper is therefore to compare both U-Net-based mapping directions using the same paired DIC and IRT dataset. The first model maps DIC-derived effective strain fields to infrared thermography data, while the second model maps infrared thermography data to DIC-derived effective strain fields. The comparison is based on quantitative error measures, visual agreement between predicted and reference fields, localisation of relevant regions, and the physical interpretation of the obtained results. By comparing both directions, the paper investigates whether the learned relation between mechanical and thermal full-field data is direction-dependent, and which mapping direction is more useful for experimental mechanics applications.

2. Materials and Methods

2.1. Experimental Data Acquisition

The experimental data used in this study were obtained from mechanical tests recorded simultaneously using a high-speed camera for DIC image acquisition and an infrared camera for thermographic measurements. The purpose of the acquisition setup was to obtain paired full-field mechanical and thermal data from the same specimen during loading. In this way, each DIC-derived effective strain field could be associated with the corresponding infrared thermography image.

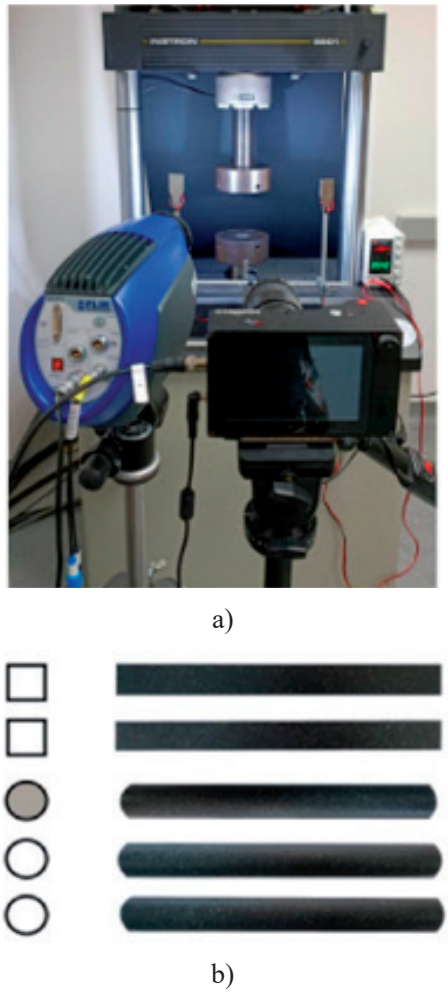


Fig. 2. Experimental setup: (a) servo hydraulic testing machine (Instron 8801, upper centre), infrared camera for temperature acquisition (FLIR SC5000MW, lower left), and high-speed camera for Digital Image Correlation measurements (Chronos 1.4, lower right); (b) aluminium alloy tube specimens, shown in empty and Ethylene–Vinyl Acetate-filled configurations.

The specimens were tested using an Instron 8801 servo-hydraulic testing machine. Loading was applied under controlled displacement conditions, with a jaw speed of 287 mm/s. During the test, the specimen surface was recorded using a Chronos 1.4 high-speed camera with a resolution of 1280 × 1024 pixels. At the same time, the thermal response of the specimen surface was recorded using a FLIR SC5000 infrared camera with a resolution of 320 × 256 pixels. Both systems were operated at a frame rate of 474 fps, allowing the rapid development of mechanical and thermal fields to be captured during loading.

For the DIC, the specimen surface seen in Fig. 2. b) was prepared with a stochastic speckle pattern suitable for op-

tical tracking [4]. The image sequence recorded by the high-speed camera was later processed to calculate displacement and strain fields. The infrared camera recorded the corresponding surface temperature field during the same loading process. Since the two systems have different spatial resolutions and measurement principles, further processing was required before the data could be used for direct full-field mapping.

2.2. Data Preprocessing

High-speed image sequences were processed using NCorr, an open-source two-dimensional local Digital Image Correlation software [5], to obtain the in-plane displacement and strain fields. The same Digital Image Correlation processing procedure and parameters as reported for this experimental dataset in our previous work [3] were used. The Eulerian–Almansi strain tensor, evaluated in the deformed configuration, was selected for strain calculation. From its normal and shear components, the two principal strains E1 and E2 were determined. An effective von Mises-type strain was subsequently adopted as the scalar measure of deformation and was calculated as:

$$E_{eff} = \sqrt{\frac{2}{3}((E_1 - E_2)^2 + E_1^2 + E_2^2)} \quad (1)$$

The resulting effective strain field was used as the mechanical full-field quantity throughout the present study. The principal NCorr processing parameters used for the five experimental datasets are summarised in Table 1.

#	1	2	3	4	5
Frames Used for DIC Processing	47	55	36	34	46
Subset Radius	16	15	17	15	16
Subset Spacing	0	0	0	0	0
Num Threads	4	4	4	4	4
Diff Norm	0.0001	0.001	0.001	0.0001	0.0001
Iterations	99	99	99	99	50
High Strain Analysis, Leap-frog Number of Steps	5	3	7	6	Off auto-propagation options
Dis-continues Analysis	On	On	On	On	On
Strain Radius	10	10	10	10	10

Table 1. NCorr analysis parameters used for each experimental dataset.

The thermographic recordings were processed to obtain the corresponding infrared thermography fields. Further processing was carried out in MATLAB. The Digital Image Correlation-derived effective strain field was used as the geometric reference for alignment. Because the optical and infrared cameras were not perfectly aligned, a small in-plane rotation was applied to the thermographic frames to correct the angular offset between the two views. The specimen region was then followed through the thermographic sequence using a specimen-centred bounding region. After cropping, the specimen was centred within the image domain so that the mechanical and thermal fields shared the same image centre. The Digital Image Correlation-derived effective strain fields were treated in the same manner, providing a common spatial reference for both modalities. The aligned fields were then resized to a common resolution of 256 × 256 pixels and stored as single-channel images. This provided spatially corresponding thermal and mechanical fields for image-to-image mapping in both directions.

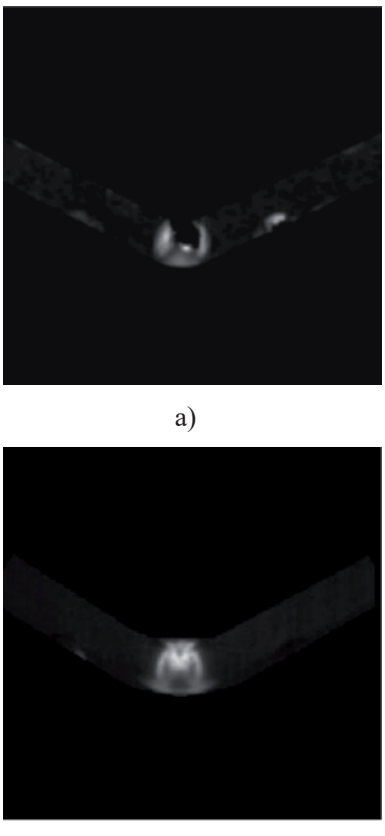
Prior to construction of the final paired dataset, the recorded sequences were screened and cleaned. Duplicate frames and non-informative frames, particularly those from the initial part of the tests before a meaningful deformation and thermal response had developed, were removed. Following this cleaning and pairing procedure, 189 corresponding Digital Image Correlation–infrared thermography image pairs remained and were used as the original dataset for model development. The data were normalised from zero to one before training to make them suitable for neural network regression. The normalisation was applied consistently within each data type.

Data set	Temperature Min	Temperature Max	Effective Strain Min	Effective Strain Max
1	19.7 °C	44.3 °C	0	4.47
2	21.1 °C	44.8 °C	0	3.96
3	20.5 °C	43.8 °C	0	4.07
4	21.3 °C	45.1 °C	0	4.34
5	20.8 °C	43.9 °C	0	4.14

Table 2. Minimum and maximum effective strain and temperature values per dataset.

The dataset consisted of 189 paired Digital Image Correlation–infrared thermography full-field images acquired from five experiments. The paired frames were divided at the individual-frame level into training, validation, and test subsets using a 70/15/15 ratio. The division was performed so that all five experiments were represented in each subset. Within each experiment, frames were also distributed across the complete loading sequence, ensuring that the training, validation, and test subsets each contained data from the early, intermediate, and later stages of deformation. The subsets were therefore not formed from separate experiments or from consecutive temporal sections of individual loading sequences. The split was performed before data augmentation, and no original image pair was repeated between subsets. Data augmentation was subsequently applied separately within each subset while preserving the spatial correspondence between the effective strain and thermographic fields. The same geometric

transformation was applied simultaneously to both images of each pair. The augmentation consisted of random rotations within ±3°, translations of up to ±5 pixels, and uniform scaling within ±3%. These transformations were selected to represent realistic image-space variations associated with small differences in camera positioning, alignment, framing and field of view, thereby reducing the dependence of the network on one exact acquisition geometry. Each original pair was augmented several times using random combinations of these transformations, with up to nine augmented versions generated from a single original pair. All augmented versions originating from a given pair remained within the same subset as the original pair, thereby preventing data leakage between the training, validation, and test sets. After augmentation, the final dataset contained 1655 paired images, comprising approximately 1158 training pairs, 248 validation pairs, and 249 test pairs. In the first direction, the DIC-derived effective strain field was used as the input and the infrared thermography image was used as the target. In the second direction, the infrared thermography image was used as the input and the DIC-derived effective strain field was used as the target. This allowed both mapping directions to be compared using the same experimental data and preprocessing procedure.



a)

b)

Fig. 3. Examples of paired input–output data used for network training: a) effective strain field obtained from DIC; b) corresponding thermal field.

2.3. U-Net Architecture and Training Strategy

A U-Net-based convolutional neural network [6] was used for both mapping directions considered in this study. The U-Net architecture was selected because it is well suited for image-to-image regression problems in which the spatial correspondence between the input and output fields must be preserved. This is particularly important for full-field experimental data, where localised regions, gradients, and spatial patterns contain relevant mechanical and thermal information.

The network follows an encoder–decoder structure. The encoder progressively extracts spatial features from the input field, while the decoder reconstructs the corresponding target field at the original image resolution. Skip connections between corresponding encoder and decoder stages transfer spatial information from the contracting path to the expanding path. These connections support the preservation of local details during reconstruction and reduce the loss of spatial information caused by successive down sampling operations.

All input and output fields were represented as single-channel images with dimensions of 256 × 256 pixels. The same U-Net architecture was used for both supervised mapping tasks to enable a direct comparison between the two mapping directions. Two models were trained independently. In the first model, the DIC-derived effective strain field was used as the input, while the corresponding infrared thermography field was used as the target. In the second model, the infrared thermography field was used as the input, while the corresponding DIC-derived effective strain field was used as the target.

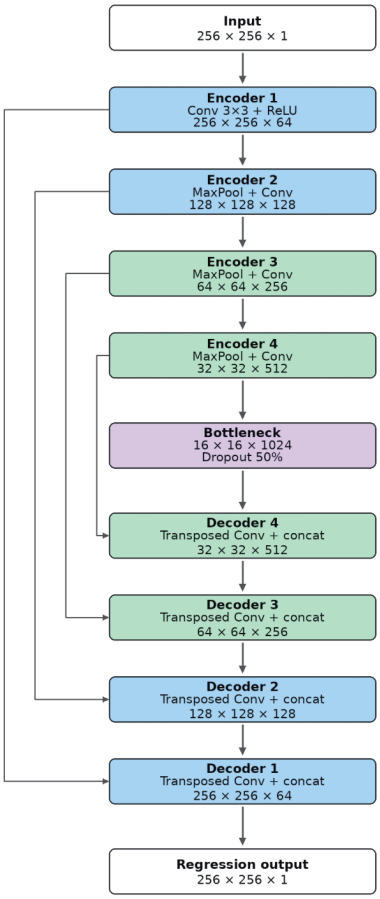


Fig. 4. Simplified schematic of the U-Net architecture used for image-to-image regression. The same encoder–decoder structure with skip connections was used for both mapping directions.

The models were implemented and trained in MATLAB using the processed paired dataset described in the previous section. Both mapping directions were trained independently using the same training configuration. The Adam optimiser was used with an initial learning rate of 1x10-4, a mini-batch size of 8, and a maximum of 400 epochs. Mean squared error was used as the loss function between the predicted field and the corresponding reference experimental field. The maximum number of epochs was used as a common upper training limit, while the training loss reached a stable region during the later stages of training. The same training procedure was applied to both mapping directions, including the same dataset division, image dimensions, input format, optimiser, learning rate, mini-batch size, number of epochs, loss function, validation strategy, and performance evaluation criteria. Consequently, the comparison was not influenced by differences in network design, data preparation, or training configuration.

Model performance was monitored using the validation subset throughout training. Following completion of the training procedure, both models were evaluated using the held-out test subset, which was not used during training. The agreement between the predicted and reference fields was quantified using Root Mean Squared Error (RMSE), Squared correlation coefficient (R2) and the Structural Similarity Index Measure (SSIM) [7]. MAE quantifies the average absolute pixel-wise difference between the predicted and reference fields, with lower values indicating smaller overall prediction error. RMSE also measures the pixel-wise prediction error, but gives greater weight to larger deviations because the errors are squared before averaging. Therefore, RMSE is more sensitive to local regions with higher prediction error. Since both MAE and RMSE are expressed in the same normalised scale as the evaluated fields, they provide a direct measure of the average reconstruction error.

SSIM evaluates the structural similarity between the predicted and reference fields by considering luminance, contrast, and spatial structure. Unlike MAE and RMSE, which are based only on pixel-wise differences, SSIM provides information about whether the spatial organisation of the reconstructed field is preserved. Values closer to 1 indicate greater structural similarity. The relationship between predicted and reference pixel values was also assessed using (R2)-based measures. The correlation-based value, (R2) was calculated as the squared correlation coefficient between the predicted and reference pixel values and describes how well both fields follow the same global trend.

The sum-of-squares-based value (R2) corresponds to the classical coefficient of determination and describes how much of the variance in the reference field is explained by the prediction. These measures were used together with MAE, RMSE, and SSIM because pixel-wise error, structural similarity, and global correlation describe different aspects of model performance. In addition to the quantitative evaluation, representative predictions were visually compared with the corresponding reference fields. This enabled the assessment of spatial distributions, gradients, and localised regions that may not be fully characterised by global numerical metrics. By using the same architecture, training strategy, and evaluation criteria for both mapping directions, the observed differences in model performance can primarily be attributed to the direction of the mapping itself.

2.4. Mapping from DIC-Derived Effective Strain to Infrared Thermography Data

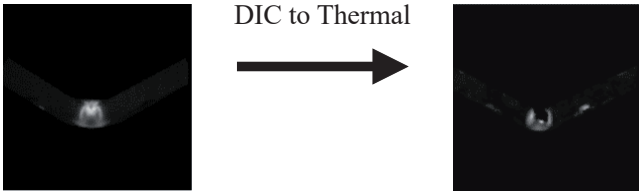
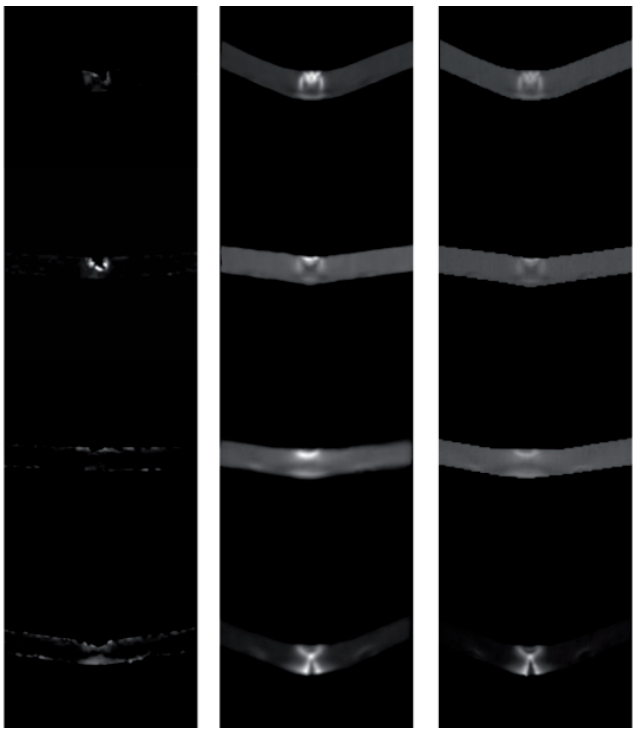


Fig. 5. Schematic representation of mapping from DIC-Derived Effective Strain to Infrared Thermography

The first mapping direction seen in Fig.6. considered in this study was the prediction of infrared thermography data from DIC-derived effective strain fields. In this configuration (see Fig. 5.), the effective strain field obtained from DIC processing was used as the input to the trained U-Net model, while the corresponding infrared thermography field was used as the reference target. This mapping direction evaluates whether the spatial information contained in the mechanical strain field can be used to reconstruct the associated thermal response of the specimen.



a) b) c)

Fig. 6. Representative results of the DIC-derived effective strain to infrared thermography mapping: a) input DIC-derived effective strain fields, b) predicted infrared thermography fields, and c) reference infrared thermography fields.

The DIC-derived effective strain to infrared thermography mapping has already been evaluated in previous work using the same general U-Net-based regression approach. The model demonstrated strong agreement between the predicted and experimentally measured thermal fields, particularly during mechanically active deformation stages, where the relationship between strain localisation and temperature variation was more pronounced.

The global test-set evaluation reported an RMSE of 0.0986, MAE of 0.0561, SSIM of 0.4262, and R^2 of 0.968. A pixel-level comparison between predicted and reference thermal fields also showed high agreement, with R^2 values of 0.985, 0.966, and 0.968 depending on the number of sampled datapoints.

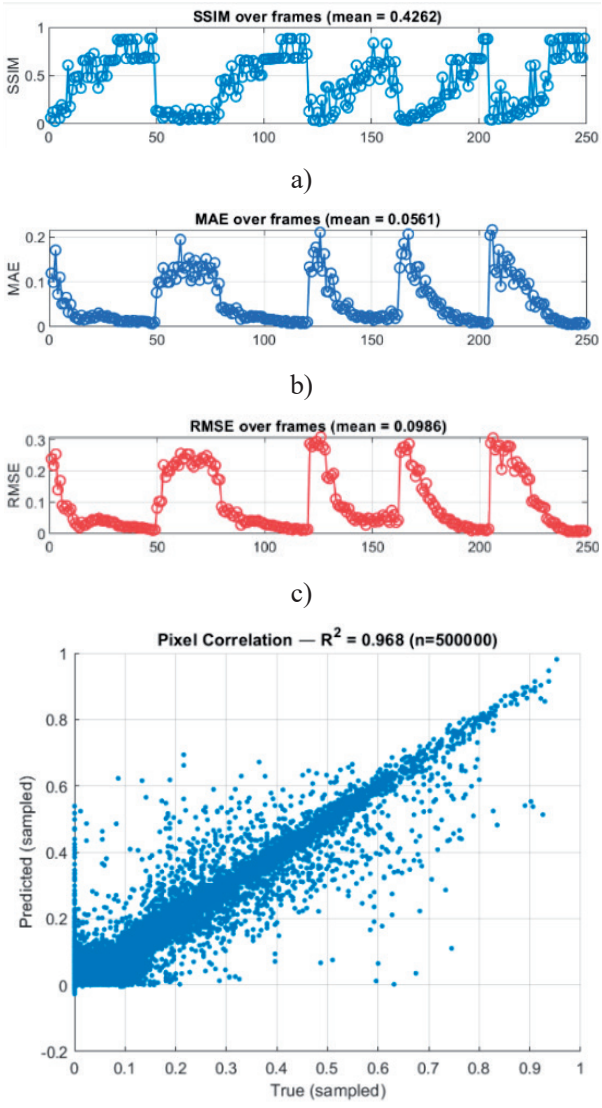


Fig.7. Quantitative evaluation of the DIC-derived effective strain to infrared thermography mapping: a) SSIM over frames, b) MAE over frames, c) RMSE over frames, and d) pixel-wise correlation between reference and predicted thermographic fields.

The results shown on Fig.7.indicate that the U-Net model was able to reproduce the dominant spatial features of the thermographic response from the DIC-derived effective strain field. The predicted thermal fields preserved the main specimen geometry and captured the regions associated with thermally active deformation. This confirms that the effective strain field contains relevant spatial information related to the thermal response under the investigated loading conditions.

However, the prediction accuracy was not uniform throughout the loading sequence. The highest errors were observed in the initial frames, where both the strain field and the thermal field contained limited spatial structure. In these nearly uniform states, the mapping between the mechanical and thermal fields is weakly defined, and small absolute deviations can produce comparatively large normalised errors. In the earliest frames, RMSE values of approximately 0.24–0.26 were reported. As deformation developed and localisation became more pronounced, the prediction accuracy improved considerably.

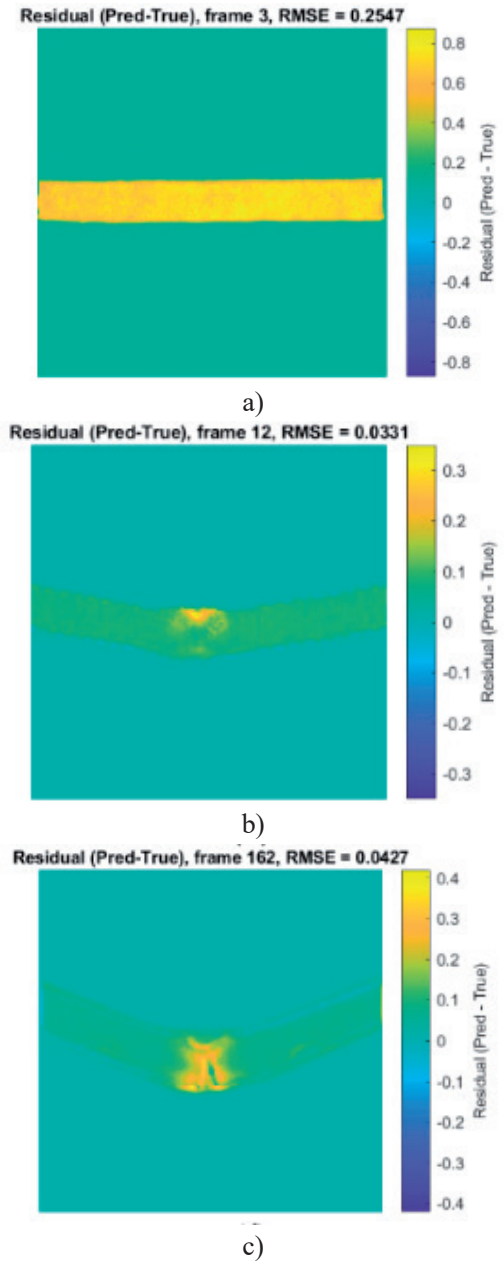


Fig.8. Residual error maps for the DIC-derived effective strain to infrared thermography mapping at selected frames: a) frame 3, b) frame 12, and c) frame 162. The residuals are calculated as the difference between the predicted and reference fields.

During the mechanically relevant part of the test sequence, approximately between frames 6 and 50, the reported MAE stabilised around 0.01–0.03, RMSE decreased to approximately, 0.02–0.04 and SSIM reached values of approximately 0.6–0.8. This behaviour indicates that the model performed best when the thermomechanical response contained clear spatial features related to deformation and damage development. Residual maps seen on Fig.8. show that the remaining discrepancies were mainly concentrated near regions with steep thermal gradients and localised deformation. These regions are expected to be more difficult to reconstruct because small spatial misalignments or local DIC noise can result in visible differences between predicted and measured thermal fields. Nevertheless, the residual fields did not indicate systematic artefacts, suggesting that the model learned a consistent relationship between the paired strain and thermal fields within the investigated experimental domain.

Overall, the DIC-derived effective strain to infrared thermography mapping demonstrated that a U-Net-based regression model can estimate the main thermal field distribution from mechanical full-field data. The results also show that the quality of the prediction depends strongly on the amount of meaningful spatial information present in the input and target fields. The mapping is most reliable during deformation stages where strain localisation and thermal response are clearly developed, while the initial nearly uniform frames remain more difficult to predict. These findings provide the reference basis for comparison with the reverse mapping direction, in which infrared thermography data are used to estimate DIC-derived effective strain fields.

2.5. Mapping from Infrared Thermography Data to DIC-Derived Effective Strain

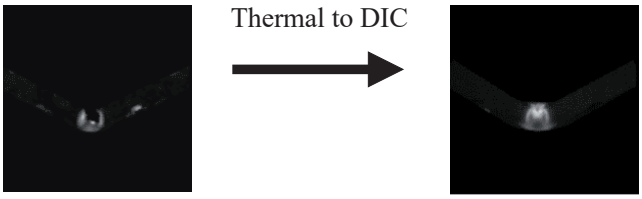


Fig. 9. Schematic representation of mapping from infrared thermography data to DIC-derived effective strain.

The second mapping direction considered (see Fig.9.) in this study was the estimation of DIC-derived effective strain fields from infrared thermography data. In this configuration, the thermographic field was used as the input to the trained U-Net model, while the corresponding DIC-derived effective strain field was used as the reference target. This mapping direction evaluates whether the thermal response of the specimen contains sufficient spatial information to estimate the underlying mechanical strain distribution.

The trained model was applied to the held-out test subset. For each test example, the network generated a predicted effective strain field from the corresponding infrared thermography image. The predicted field was then compared with the DIC-derived reference field from the same time frame. Obtained results seen on Fig. 10. show that the U-Net model was able to estimate the general distribution of the DIC-derived effective strain field from the thermographic input. The predicted fields reproduced the overall specimen response and followed the main spatial trends observed in the reference strain fields. This indicates that the infrared thermography data contain information related to the mechanical deformation field under the investigated loading conditions.

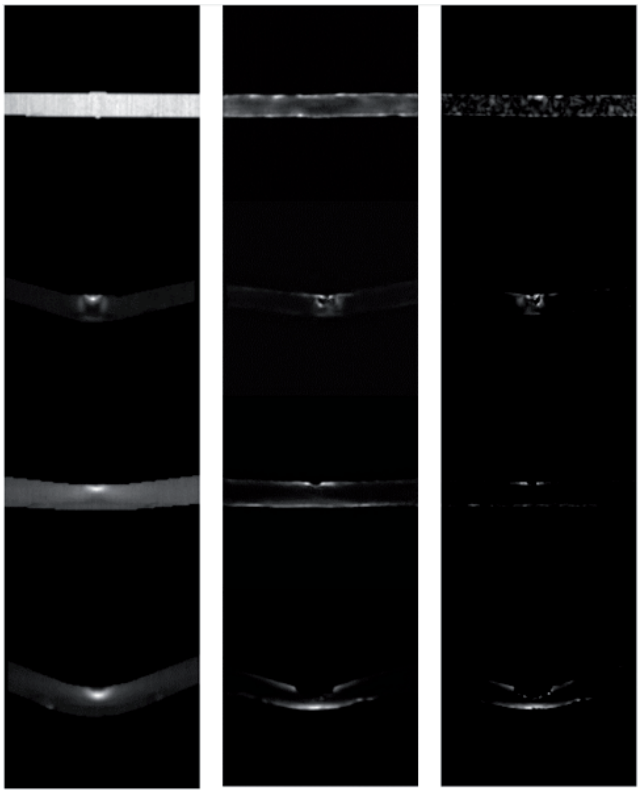
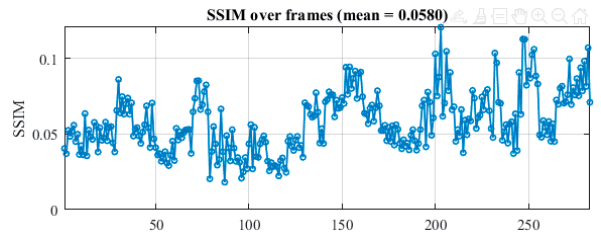


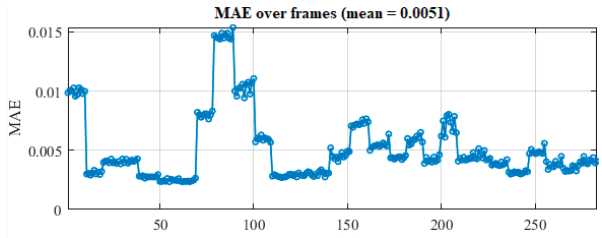
Fig. 10. Representative results of the infrared thermography to DIC-derived effective strain mapping: a) input infrared thermography fields, b) predicted DIC-derived effective strain fields, and c) reference DIC-derived effective strain fields.

The numerical evaluation seen on Fig.11. showed that the average prediction error remained relatively low. The mean RMSE over the analysed frames was 0.0188, while the mean MAE was 0.0051. The frame-wise error curves indicate that the prediction error was not constant throughout the sequence, with increased errors observed in specific frame intervals. These intervals correspond to parts of the test sequence where the strain distribution changed more rapidly or where the thermal information was less directly representative of the effective strain field. The global sampled-pixel comparison also showed a clear positive relationship between the predicted and reference DIC-derived effective strain values. For 600000 sampled pixels, the correlation-based coefficient of determination was R^2=0.692. This value indicate that the model captured a substantial part of the global relationship between the thermographic input and the corresponding mechanical strain response.

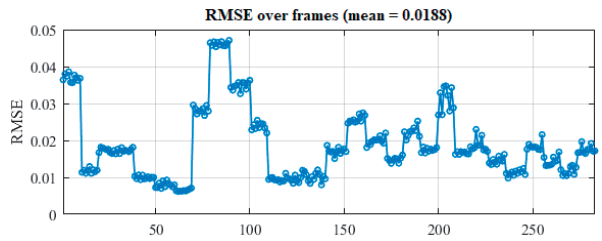
The SSIM values were considerably lower than might be expected from the pixel-wise error metrics, with a mean



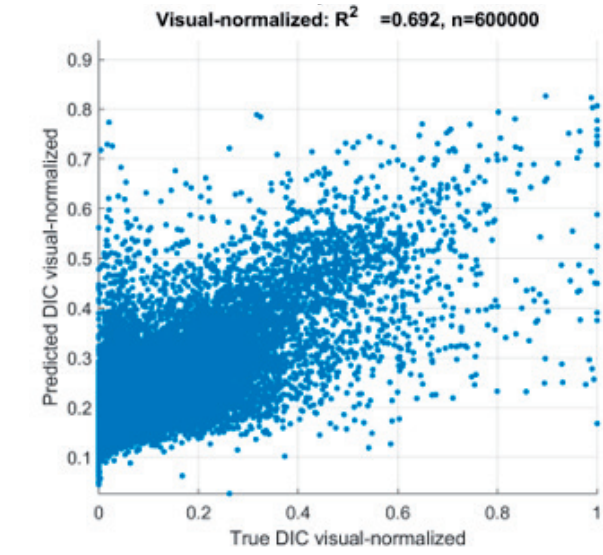
a)



b)



c)



d)

Fig.11. Quantitative evaluation of the infrared thermography to DIC-derived effective strain mapping: a) SSIM over frames, b) MAE over frames, c) RMSE over frames, and d) pixel-wise correlation between reference and predicted DIC-derived effective strain fields.

value of 0.0580 over the analysed frames. Although the model achieved relatively low average pixel-wise errors, the predicted fields did not fully reproduce the structural details of the DIC-derived effective strain fields. This difference is not contradictory, as the metrics evaluate different aspects of the prediction. RMSE and MAE quantify the average magnitude of the pixel-wise error over the complete field, whereas SSIM is more sensitive to local spatial structure, contrast, and the arrangement of features. Consequently, the model can reproduce the general strain magnitude and broad spatial distribution while still obtaining a low SSIM if narrow localisation zones are shifted, widened, smoothed, or predicted with lower peak strain values than the reference field.

A further contribution to this behaviour is the tendency of the U-Net reconstruction to smooth local features, which was also observed in the opposite mapping direction. This smoothing has a comparatively limited influence on the overall pixel-wise error but can substantially affect the structural similarity of fields containing sharp gradients and narrow strain-localisation zones. This effect is particularly important for the thermal-to-DIC mapping, since the target effective strain fields contain more sharply localised features than the comparatively smoother thermographic input fields.

The residual map for frame 142 in Fig. 12 shows that the prediction error is mainly concentrated within the specimen region, while the surrounding background remains close to zero. This indicates that the model does not introduce significant artefacts outside the mechanically relevant area. The largest residuals occur near the central deformation/localisation zone, where the DIC-derived effective strain field contains sharper gradients and more localised features. The presence of neighbouring positive and negative residual regions suggests that part of the error is related to small spatial mismatches between the predicted and reference strain distributions rather than to a uniform overprediction or underprediction. Overall, the residual map confirms that the thermal-to-DIC model captures the general strain pattern but has difficulty reproducing localised strain details with high spatial accuracy.

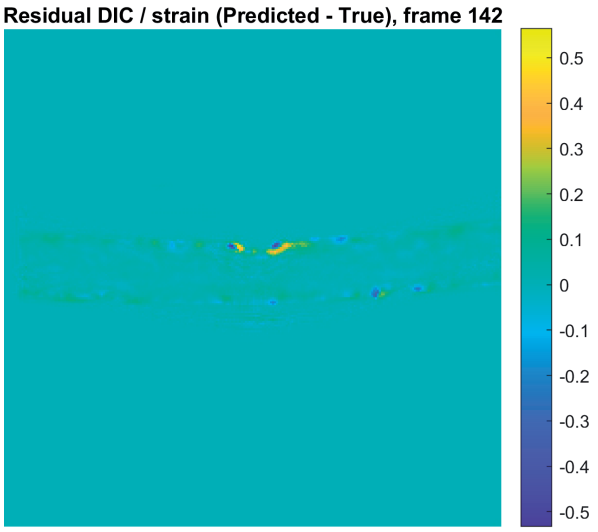


Fig.12. Residual error map for the infrared thermography to DIC-derived effective strain mapping at frame 142. The residual is calculated as the difference between the predicted and reference strain fields.

Overall, the infrared thermography-to-DIC-derived effective strain mapping demonstrated that a U-Net-based model can estimate the main mechanical strain distribution from thermal full-field data. The relatively low RMSE and

MAE values indicate good average pixel-wise agreement, while the low SSIM values show that the reconstruction of detailed spatial strain structures remains challenging. The predicted fields can therefore be considered representative of the general mechanical response and broad strain distribution, but not as quantitatively accurate reconstructions of local strain concentrations. In particular, the method should not be considered a replacement for direct DIC measurements where accurate peak strain values, strain gradients, or the detailed geometry of localisation zones are required. The results nevertheless indicate that the thermal field contains useful information about the mechanical response, while also confirming that the reverse mapping is limited by the indirect and non-unique relationship between temperature evolution and effective strain localisation

2.6. Comparison of Both Mapping Directions

The two mapping directions were compared in order to evaluate whether the learned relationship between DIC-derived effective strain fields and infrared thermography data is direction-dependent. Although both models were based on the same U-Net architecture and trained using paired full-field data, the two tasks are not physically equivalent. The first direction estimates the thermal response from a mechanical strain field, while the second direction estimates the mechanical strain field from the measured thermal response. Therefore, the comparison must consider not only numerical accuracy, but also spatial reconstruction quality and physical interpretability.

2.6.1. Quantitative Comparison

The DIC-derived effective strain to infrared thermography mapping showed strong global agreement in the previously reported evaluation, with RMSE = 0.0986, MAE = 0.0561, SSIM = 0.4262, and R^2 = 0.968 on the independent test set. During the mechanically active part of the sequence, where deformation and temperature localisation were more pronounced, the model performance improved considerably, with RMSE values decreasing to approximately 0.01–0.03, MAE values stabilising around 0.02–0.04, and SSIM values reaching approximately 0.6–0.8.

For the reverse mapping direction, from infrared thermography data to DIC-derived effective strain, the mean RMSE over the analysed frames was 0.0188 and the mean MAE was 0.0051. The global sampled-pixel comparison produced R^2=0.692 for 600000 sampled pixels. However, the mean SSIM was substantially lower, with a value of 0.0580, indicating limited structural similarity between the predicted and reference effective strain fields.

Mapping direction	RMSE	MAE	SSIM	R^2
DIC to Thermal	0.0986	0.0561	0.4262	0.968
Thermal to DIC	0.0188	0.0051	0.0580	0.692

Table 3. Quantitative comparison of the DIC-derived effective strain to infrared thermography and infrared thermography to DIC-derived effective strain mapping directions.

Although the thermal-to-DIC mapping produced lower RMSE and MAE values, these values should not be interpreted as a direct indication that this direction is superior. The two models predict different physical quantities with different spatial distributions, dynamic ranges, and normalisation behaviour. Therefore, RMSE and MAE are useful for evaluating each model individually, but they are not fully equivalent across mapping directions. A more meaningful comparison is obtained by considering the complete set of metrics together with the visual agreement between predicted and reference fields.

2.6.2. Qualitative Comparison

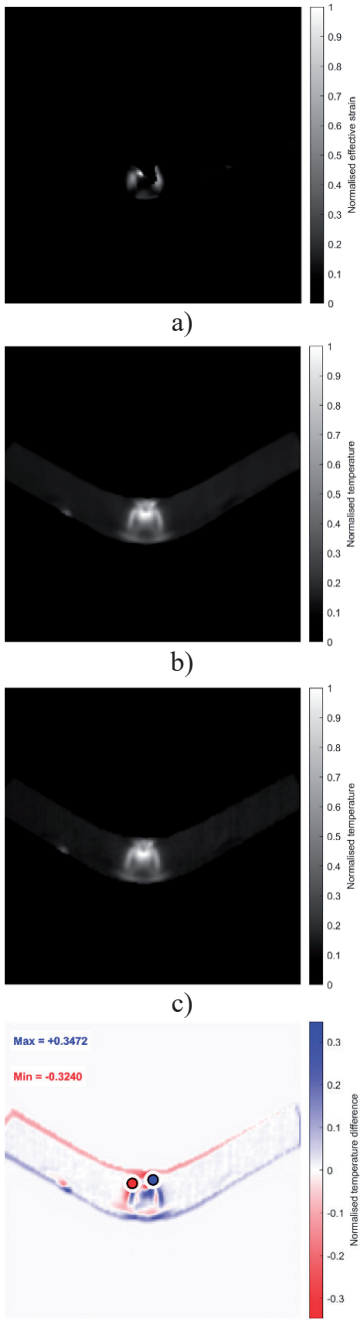


Fig.13. Representative DIC-to-thermal mapping result: a) DIC-derived effective strain input, b) predicted thermographic field, c) reference thermographic field, and d) difference between the predicted and reference thermographic fields.

Visual comparison provides additional insight into the behaviour of both models. In the DIC-derived effective strain to infrared thermography mapping on Fig.6., the predicted thermal fields reproduced the general thermal distribution and the dominant regions of temperature variation.

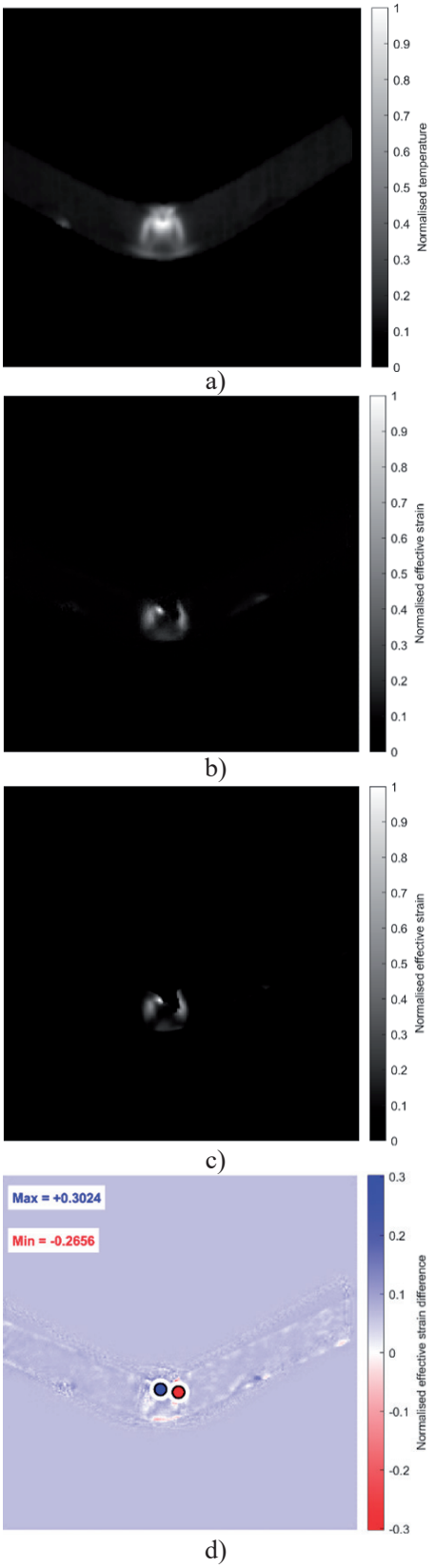


Figure 14. Representative thermal-to-DIC mapping result: a) infrared thermography input, b) predicted DIC-derived effective strain field, c) reference DIC-derived effective strain field, and d) difference between the

The model was particularly effective in frames in which deformation localisation produced a clear thermal response. To examine the behaviour in the region of significant deformation in more detail, Fig. 13. presents a representative DIC input together with the predicted and reference thermal fields and their difference map. The predicted and reference fields are shown using identical normalised colour-scale limits, allowing their spatial distributions and magnitudes to be compared directly. The model reproduces the position and broader extent of the central thermal response, while the main residuals remain concentrated around this localisation region. For the presented frame, the maximum positive and negative differences are approximately +0.347 and −0.324, respectively. The neighbouring positive and negative residuals indicate local differences in the magnitude and spatial extent of the predicted thermal response rather than a uniform over- or underprediction across the specimen. Outside the principal localisation region, the differences are considerably smaller. This confirms that the model captures the broader thermal response well, while the largest errors occur in regions characterised by steep spatial gradients and strongly localised deformation.

In the reverse mapping direction shown in Fig. 14, the model was able to estimate the general distribution of the DIC-derived effective strain field from the thermographic input. However, the reconstruction of fine localised strain features was more challenging. This is reflected in the low SSIM values, which indicate limited structural similarity between the predicted and reference strain fields despite relatively low average pixel-wise errors. The predicted fields therefore captured the broader deformation trend more reliably than the detailed strain localisation pattern. A more detailed comparison of a representative high-deformation frame is presented in Fig. 14. The predicted field reproduces the characteristic V-shaped distribution of the specimen and correctly identifies the central region in which the highest strain localisation occurs. The difference map nevertheless reveals a predominantly light-blue residual over much of the field, corresponding approximately to a positive difference of 0.05–0.10 on the normalised scale. This indicates a slight general tendency of the model to overpredict the effective strain magnitude. More pronounced discrepancies are concentrated around the central deformation region, where the maximum positive and negative differences reach approximately +0.302 and −0.266, respectively. Importantly, the residual pattern largely follows the geometry of the specimen rather than appearing randomly throughout the image. The neighbouring positive and negative extrema around the central region indicate differences in the precise position, width and magnitude of the reconstructed strain concentration. Thus, the model retains the overall shape and location of the mechanical response, while reconstruction of the sharp local strain distribution remains less accurate.

The difference between the two mapping directions is therefore important. Thermal fields are generally smoother and more spatially continuous than DIC-derived effective strain fields. As a result, predicting a thermal field from a strain input may be more favourable for an encoder–decoder network because the target distribution contains broader gradients and fewer sharply localised details. In

contrast, DIC-derived effective strain fields can contain narrow localisation zones, high-gradient regions and local variations introduced by DIC processing. These features are more difficult to reconstruct from thermal data alone.

An additional factor is the difference in the native spatial resolution and information content of the two measurement modalities. The DIC-derived strain fields originate from higher-resolution optical images, whereas the thermographic measurements were acquired at a lower spatial resolution and exhibit smoother spatial variations. Although both modalities were resized to 256 × 256 pixels before training, this resizing does not recover fine spatial information that was absent from the original thermographic measurements. Consequently, the DIC-to-thermal mapping transforms a comparatively detailed mechanical field into a smoother thermal field, whereas the reverse direction requires the model to infer finer local strain features from a spatially coarser thermal representation. This asymmetry provides an additional explanation for the greater difficulty observed in the thermal-to-DIC mapping.

2.6.3. Physical Interpretability

The comparison also shows that the two mapping directions have different physical interpretations. Mapping from DIC-derived effective strain to infrared thermography data investigates whether the mechanical deformation field contains sufficient information to estimate the corresponding thermal response. This direction is physically meaningful because local deformation, plastic dissipation, and damage development can contribute to temperature changes. However, the thermal field is also influenced by heat transfer, emissivity, surface conditions, camera response, and temporal effects. Therefore, the thermal response cannot be considered a unique function of the instantaneous strain field alone.

The reverse direction, from infrared thermography data to DIC-derived effective strain, has a different interpretation. It investigates whether the measured thermal response can be used to infer the underlying mechanical strain field. This is a more indirect problem, because temperature variations are a consequence of several coupled processes and do not uniquely define the mechanical state. The obtained results show that the thermal field contains useful information about the mechanical response, but the low SSIM values suggest that detailed strain localisation cannot be fully reconstructed from thermal data alone under the present conditions.

The comparison therefore indicates that the relationship between DIC-derived effective strain and infrared thermography data is not symmetric from a data-driven perspective. The DIC-to-IRT model showed stronger structural agreement for reconstructing the thermal field, while the IRT-to-DIC model achieved low average pixel-wise errors but weaker structural similarity. This suggests that the mapping direction strongly affects both the numerical performance and the physical meaning of the predicted field.

2.6.4. Practical Relevance

From a practical point of view, both mapping directions have potential applications, but they address different experimental needs. The DIC-derived effective strain to infrared thermography mapping may be useful in cases where thermal information is unavailable, incomplete, or difficult to acquire. If a model has been trained for a specific material, geometry, and loading configuration, it may provide an estimate of the expected thermal field based on DIC-derived mechanical data.

The infrared thermography to DIC-derived effective strain mapping is particularly interesting because it explores the possibility of estimating mechanical full-field information from thermal measurements. This may be relevant in experimental setups where conventional DIC is difficult to apply, for example due to limited optical access, poor lighting conditions, speckle pattern degradation, or camera placement restrictions. In such cases, thermal imaging could provide an indirect source of information about the mechanical response.

However, the present results indicate that thermal-to-DIC mapping should be interpreted with caution. The model can estimate the general strain distribution, but the reconstruction of detailed localised strain structures remains limited. Therefore, this approach should not be considered a direct replacement for DIC. Instead, it may be more appropriate as a complementary method for approximate strain-field estimation, experimental screening, or multimodal data fusion.

2.6.5. Limitations

Several limitations must be considered when interpreting the comparison. First, both models were trained and evaluated using data from the same experimental framework. The learned mappings are therefore specific to the investigated material, specimen geometry, loading configuration, acquisition setup, and preprocessing procedure. Generalisation to other experimental conditions cannot be assumed without additional validation.

Second, the two mapping directions predict different target quantities. Direct comparison of RMSE and MAE values is therefore limited, even when the data are normalised. The metrics are useful for assessing prediction quality within each task, but they do not provide a complete measure of physical equivalence between the two models.

Third, the thermal and strain fields differ in spatial character. Thermographic fields are generally smoother, while DIC-derived effective strain fields may contain sharper gradients, localisation zones, and processing-related noise. This difference affects SSIM and visual reconstruction quality, particularly in the thermal-to-DIC direction.

Finally, both mappings are data-driven and do not explicitly include the governing thermomechanical equations. The models learn statistical relationships between paired fields, but they do not enforce heat transfer, material constitutive behaviour, or energy balance. Future work should therefore include larger datasets, additional loading cases, temporal modelling, and physics-informed constraints in order to improve generalisation and physical consistency.

3. Conclusion

This paper compared two U-Net-based mapping directions between DIC-derived effective strain fields and infrared thermography data. The first direction used effective strain fields as input to predict thermographic fields, while the second used thermographic fields as input to estimate effective strain fields. Both models were evaluated using the same paired experimental dataset and the same general network architecture.

The results show that both directions can be learned to a certain extent, but they are not equivalent. The DIC-to-IRT mapping reproduced the main thermal field distribution and showed stronger structural agreement with the reference thermographic data. This indicates that the DIC-derived effective strain field contains relevant spatial information associated with the measured thermal response.

The reverse mapping, from IRT to DIC-derived effective strain, also produced useful estimates of the mechanical field. The model achieved low average pixel-wise errors, with mean RMSE and MAE values of 0.0188 and 0.0051, respectively. However, the low mean SSIM value shows that the detailed spatial structure of the strain field was not fully reconstructed. Therefore, this direction is better interpreted as an approximate estimation of the general strain distribution rather than a full replacement for DIC.

Overall, the comparison confirms that the relationship between mechanical and thermal full-field data is direction-dependent. The DIC-to-IRT direction is more suitable for reconstructing smoother thermographic fields, while the IRT-to-DIC direction is more challenging because strain fields contain sharper localisation zones and stronger spatial gradients. Future work should include larger datasets, additional loading cases, and temporal or physics-informed models to improve the generalisation and physical consistency of the learned mappings.

4. References

[1] B. Pan, K. Qian, H. Xie, and A. Asundi, “Two-dimensional digital image correlation for in-plane displacement and strain measurement: a review,” *Meas. Sci. Technol.*, vol. 20, no. 6, p. 62001, Apr. 2009, doi: 10.1088/0957-0233/20/6/062001.

[2] A. Chrysochoos, “Infrared thermography applied to the analysis of material behavior: a brief overview,” *Quant. Infrared Thermogr. J.*, vol. 9, no. 2, pp. 193–208, 2012, doi: 10.1080/17686733.2012.746069.

[3] A. Grebo, N. Novak, B. Panić, and L. Krstulović-Opara, “A Deep Learning Framework for Full-Field Thermal Field Distribution Prediction from Digital Image Correlation Strain Measurements,” *Applied Sciences*, vol. 16, no. 1, 2026, doi: 10.3390/app16010460.

[4] D. Lecompte *et al.*, “Quality assessment of speckle patterns for digital image correlation,” *Opt. Lasers Eng.*, vol. 44, no. 11, pp. 1132–1145, Nov. 2006, doi: 10.1016/j.optlaseng.2005.10.004.

[5] J. Blaber, B. Adair, and A. Antoniou, “Ncorr: Open-Source 2D Digital Image Correlation Matlab Software,” *Exp. Mech.*, vol. 55, no. 6, pp. 1105–1122, Jul. 2015, doi: 10.1007/s11340-015-0009-1.

[6] P. and B. T. Ronneberger Olaf and Fischer, “U-Net: Convolutional Networks for Biomedical Image Segmentation,” in *Medical Image Computing and Computer-Assisted Intervention – MICCAI 2015*, J. and W. W. M. and F. A. F. Navab Nassir and Hornegger, Ed., Cham: Springer International Publishing, 2015, pp. 234–241.

[7] Zhou Wang, A. C. Bovik, H. R. Sheikh, and E. P. Simoncelli, “Image quality assessment: from error visibility to structural similarity,” *IEEE Transactions on Image Processing*, vol. 13, no. 4, pp. 600–612, Apr. 2004, doi: 10.1109/TIP.2003.819861.